



Research Article

<https://doi.org/10.1631/jzus.A2300072>



Constitutive modelling of concrete material subjected to low-velocity projectile impact: insights into damage mechanism and target resistance

Shen LIU^{1,2}, Xieping HUANG^{1,2✉}, Xiangzhen KONG³, Qin FANG³

¹Center for Hypergravity Experiment and Interdisciplinary Research, Zhejiang University, Hangzhou 310058, China

²Institute of Geotechnical Engineering, Zhejiang University, Hangzhou 310058, China

³State Key Laboratory of Disaster Prevention & Mitigation of Explosion & Impact, Army Engineering University of PLA, Nanjing 210007, China

Abstract: This paper presents a numerical study to improve the understanding of the complex subject of penetration and perforation of concrete targets impacted by low-velocity projectiles. The main focus is on the damage mechanisms and the major factors that account for the target resistance of the concrete. An improved continuous surface cap model recently proposed was employed. The model was first equipped with element erosion criteria and was adequately validated by comparisons with ballistic experiments. Comprehensive numerical simulations were carried out where the individual influence of tensile, shear, and volumetric behaviors (pore collapse) of a concrete target on its ballistic performance was investigated. Results demonstrated that cratering on the front face and scabbing on the rear face of the concrete target were mainly dominated by its tensile behavior. The major target resistance came from the second tunneling stage which was primarily governed by the shear and volumetric behaviors of the concrete. Particularly, this study captured the pore collapse-induced damage phenomenon during the high-pressure tunneling stage, which has been extensively reported in experiments but has usually been neglected in previous numerical investigations.

Key words: Penetration; Perforation; Damage mechanism; Target resistance; Projectile impact; Pore collapse

1 Introduction

Concrete is a frequently used material in military and civil engineering that may undergo impact and blast loads. Failure modes of concrete structures under these dynamic loads and the underlying damage mechanisms are thus of great interest and have attracted intensive attention for many years. For impact loads such as the penetration into concrete, numerous investigations (Rajput et al., 2018; Goswami et al., 2019; Liu et al., 2021; Xu et al., 2021) have been carried out during the last decades to enhance the understanding of this complicated problem. This study focuses mainly on the penetration problem with a numerical study

performed to investigate the ballistic performance of concrete targets impacted by low-velocity projectiles.

It is well acknowledged that the penetration into concrete comprises, in general, two relevant problems (Hanchak et al., 1992; Yankelevsky, 1997). The first problem is penetration into a relatively thin target where the target can be perforated by the projectile with a residual velocity; the second problem is penetration into a sufficiently thick target where the projectile will be stopped within the target with a penetration depth considerably smaller than the target thickness such that no rear face effects can be observed. The two related problems have much in common but they are significantly different as well. In this study, both the problems will be considered. To make it easy to follow, we will refer to the first problem as perforation and the second problem as penetration.

In studies on the penetration and perforation problems (Hanchak et al., 1992; Yankelevsky, 1997; Huang et al., 2005; Leppänen, 2006; Wang et al.,

✉ Xieping HUANG, huangxieping@zju.edu.cn

Shen LIU, <https://orcid.org/0000-0003-3246-7011>

Xieping HUANG, <https://orcid.org/0000-0002-0961-9745>

Received Feb. 8, 2023; Revision accepted May 4, 2023;

Crosschecked Nov. 21, 2023

© Zhejiang University Press 2024

2007; Forquin et al., 2008, 2015; Kong et al., 2016), typical failure modes of a concrete target can be commonly observed. Fig. 1 schematically illustrates the failure modes of a concrete target under perforation. In general, the whole perforation process can be divided into three stages. The first stage is associated with the entrance phase of the projectile, where cratering on the front face of the target can be observed. The second stage refers to the tunneling region, where a tunnel in the center with a size approximate to the projectile diameter will be created. The third stage is related to the exit phase of the projectile, where scabbing on the rear face is visible. For the penetration case, the third stage is generally absent and for some perforation cases with very thin targets, only the first and the third stages can be found and, the second tunneling stage is not present.

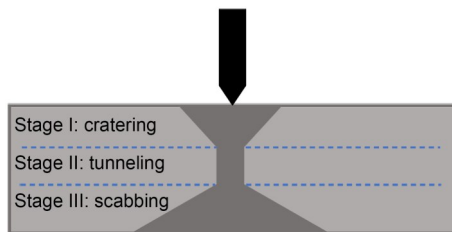


Fig. 1 Typical three-stage failure modes of a concrete target under perforation

The first point for discussion in this study is the damage mechanism behind the failure mode of the target during each stage. Discussions related to this topic are abundant (Hanchak et al., 1992; Yankelevsky, 1997; Huang et al., 2005; Leppänen, 2006; Wang et al., 2007; Chen et al., 2008; Forquin et al., 2008, 2015; Li et al., 2013; Kong et al., 2016; Xing et al., 2020); however, the opinions are quite controversial. In general, the second, tunneling, stage is well acknowledged to be associated with shear strength–pressure relations, since a triaxial compression stress state with high confining pressure is observed in the tunnel (Yankelevsky, 1997; Forquin et al., 2008, 2015). However, opinions concerning the controlled damage mechanisms in the first and the third stages are divided. On the one hand, Hanchak et al. (1992) pointed out that both the cratering and scabbing were produced by tensile spallation. Kong et al. (2016) also suggested that both the cratering and scabbing were tension-dominated phenomena. On the other hand, Wang et al. (2007) believed that the impacted area on the front face was

primarily under compression and may fail due to high pressure, with the cratering on the front face resulting from the severe ‘crushing-stress’ together with a partially reflected tensile stress wave. Forquin et al. (2015) also concluded from their experimental results and numerical simulations that the cratering was mainly related to the ‘confined behavior’ rather than the tensile behavior of the target. Moreover, studies (Hanchak et al., 1992; Huang et al., 2005; Leppänen, 2006; Wang et al., 2007; Forquin et al., 2015; Kong et al., 2016) indicated that the scabbing on the rear face was dominated by the reflected tensile stress wave. In addition, researchers (Chen et al., 2008; Li et al., 2013; Xing et al., 2020) believed that both the shear plugging and tensile spallation appeared almost at the same time on the rear face of the target and that shear failure rather than tensile failure was dominant.

Based on the literature review presented, the damage mechanisms are arguable and further efforts are required. Also, at least two aspects should be considered. Firstly, the damage mechanism that controls the formation of the cratering and the scabbing is not clear. To approach this issue, ballistic experiments or numerical simulations with well-designed concrete targets are needed. The targets in a control group should have different mechanical behaviors in a certain aspect and identical behaviors in the other aspects, so that the individual influence of the different mechanical behaviors of the target during different stages can be acquired. Secondly, although a triaxial compression stress state with high confining pressure is well acknowledged in the tunneling region, understanding of the damage mechanism during this stage is still inadequate. For instance, the damage mechanism due to pore collapse under high pressure is commonly neglected in most of the existing numerical studies. However, Holmquist et al. (1993) pointed out that pore collapse under high pressure will cause a great loss of cohesive strength of materials. This phenomenon has also been mentioned in (Forquin et al., 2008). In addition, more recently, the experimental results from Cui et al. (2017) indicate that over 50% of the material strength and modulus have been lost after the material has suffered a hydrostatic loading test with the pressure up to 500 MPa. Considering the high confining pressure observed during the second tunneling stage, damage due to pore collapse will be very severe there and must be considered in the numerical simulations.

Besides the damage mechanisms, opinions upon the major factor that accounts for the target resistance are also rather controversial and in some cases conflict with the views on the damage mechanisms behind the failure modes of the concrete target. For instance, although many researchers (Leppänen, 2006; Kong et al., 2016) believed that the cratering and the scabbing were tension-dominated phenomena, they still suggested that the target resistance was mainly determined by the compressive behavior and the strain-rate-dependent responses of the concrete in compression; the contribution of the tensile behavior was neglected. However, these conclusions were questioned by Forquin et al. (2015) through a set of ballistic experiments and numerical simulations. Forquin et al. (2015) concluded from their results that tensile behavior can strongly influence the concrete target resistance. Beppu et al. (2008) also pointed out that tensile behavior was important.

There have also been many attempts made to propose analytical models (Durban and Masri, 2004; Masri and Durban, 2005; Rosenberg and Dekel, 2010; Rosenberg and Kositski, 2016; Kong et al., 2017a, 2017b) and empirical formulae (Forrestal et al., 1994, 1996) to predict the target resistance. More details are in the reviews (Li et al., 2005; Yankelevsky, 2017). These attempts can be covered generally by two kinds of models. The first kind of models are those where the unconfined compressive strength of the target appeared to be the major factor of the target resistance (Rosenberg and Dekel, 2010; Rosenberg and Kositski, 2016). In those models, the predicted penetration depth of the projectile was inversely proportional to the square root of the unconfined compressive strength. However, experimental observations (Hanchak et al., 1992) have shown that an increase in the unconfined compressive strength of a factor of three had a very limited influence on the target resistance for impacting velocities ranging between 300 and 1100 m/s. Experimental studies (Yankelevsky, 2017) have also revealed that concrete targets of similar unconfined compressive strength demonstrated different ballistic resistances depending on their different concrete compositions. These findings indicated that unconfined compressive strength was insufficient to be the major factor of the target resistance. Researchers (Forquin et al., 2008, 2015; Kong et al., 2017a, 2017b) also argued that unconfined compressive strength was not the major factor. These debates led to another kind of

analytical model: the dynamic cavity model (Durban and Masri, 2004; Masri and Durban, 2005; Kong et al., 2017a, 2017b). In the dynamic cavity model, much more complicated mechanical behaviors of the target were required to describe the target resistance, including deviatoric behaviors (shear strength–pressure relations) and volumetric behaviors (volumetric strain–pressure relations).

In light of the literature review, more efforts are still required to understand the major factor that accounts for the target resistance and that is the second point that the current study will discuss. More attention should be focused on at least two aspects related to the target resistance. Firstly, whether the unconfined compressive strength is sufficient or the complex shear and volumetric behaviors considered in the analytical models are necessary, should be further discussed. Secondly, although tensile behaviors can strongly influence the formation of the cratering and the scabbing, the influence of tensile behaviors on target resistance has been commonly neglected and needs to be further investigated.

This study aims at enhancing the understanding of these two points especially in the detailed four aspects discussed above. It must be pointed out that to explore these issues experimentally needs well-designed concrete targets and a high number of experiments to improve the statistics; these are not easy and are generally expensive. Numerical simulation naturally has advantages in dealing with these issues thanks to the rapid development of computational power, numerical methods, and constitutive models. As for the constitutive models for studying the complex penetration and perforation problems, the physical mechanisms of the concrete due to microcracks and pores as well as their combinations should be considered. In this study, the concrete model recently proposed by Huang et al. (2021) is adopted with minor modifications. This model can well capture the mechanical behaviors of rock and concrete materials under complex stress states. In particular, three damage mechanisms are considered: hydrostatic damage due to pore collapse under high pressure, shear damage due to shear-induced microcracking, and tensile damage due to tensile microcracking. This model will first be equipped with element erosion criteria and then sufficiently validated by comparisons with ballistic experiments before the numerical study.

It should be mentioned that this study focuses on the ballistic performances of conventional concrete materials. Fiber-reinforced concrete and ultrahigh-performance concrete are not included. In addition, a plastic-damage constitutive model within the framework of the finite element method is employed to predict the different damage phenomena (tensile, shear, and volumetric) during the projectile's impact on the concrete material. The finite element method, incorporating a well-developed constitutive material model, has been frequently used in predicting the damage and failure of concrete materials subjected to impact and blast loadings. However, there are also many other numerical methods, such as the discrete cohesive zone model (Feng et al., 2018; de Maio et al., 2022) or the phase field method (Nguyen et al., 2022), that have been proposed and show good performances in capturing crack patterns and failure modes in concrete materials. These numerical methods provide good alternatives and can also be considered in the future.

The remainder of this paper is structured as follows: in Section 2, a brief description of Huang et al. (2021)'s concrete model will be presented; in Section 3, Huang et al. (2021)'s concrete model will be fully validated with inclusion of parameter calibrations, element erosion criterion effects, mesh size effects, and comparisons with ballistic experiments; in Section 4, a numerical study will be presented where the individual influence of the tensile, volumetric, and shear behaviors of the target on ballistic performance will be investigated; in Section 5, there is a discussion upon the two main points especially in respect of the detailed four aspects mentioned above, and some conclusions are drawn.

2 Constitutive model

A brief introduction to Huang et al. (2021)'s concrete model is presented in this section, including the plastic model and damage model. With minor modifications, this concrete model will be adopted for the numerical study.

2.1 Plastic model

In Huang et al. (2021)'s concrete model, a three-invariant yield function f is used to trigger the initiation of plasticity, which is formulated as:

$$f = J_2 - r'^2 F_f^2 F_c, \quad (1)$$

where J_2 is the second invariant of the deviatoric stress tensor. $Y = r'^2 F_f^2 F_c$ is defined as the failure function, which comprises three different portions, i.e., r'^2 , F_f^2 , and F_c . F_f is the fracture function used to describe the shear strength under triaxial compression stress states. F_c is the cap function used to account for the shear strength decrease due to pore collapse under high pressure. r' is the ratio of the current meridian to the compressive meridian, which is used to allow for the Lode-angle dependence.

In Huang et al. (2021)'s concrete model, the fracture function F_f is defined as

$$F_f = \begin{cases} \frac{\sqrt{3}}{2\psi}(P+T), & 0 \leq P < f_c/3, \\ \frac{\sqrt{3}}{3} \left(f_c + \frac{P-f_c/3}{a_1+a_2P} \right), & P \geq f_c/3, \end{cases} \quad (2)$$

where P denotes the hydrostatic pressure. f_c is the unconfined compressive strength and T is the unconfined tensile strength. a_1 and a_2 are strength parameters which should be calibrated through the triaxial compression test data. ψ represents the ratio of tensile meridian to compressive meridian, which is related to P . The piecewise function ψ for concrete materials suggested in (Nguyen et al., 2022) is adopted in this study, which reads as:

$$\psi(P) = \begin{cases} 0.5, & P=0, \\ 0.5 + 1.5T/f_c, & P = \frac{f_c}{3}, \\ 1.15 / \left[1 + 1.3 / (3a_1 + 2.3a_2 f_c) \right], & P = \frac{2.3f_c}{3}, \\ 0.753, & P = 3f_c, \\ 1, & P \geq 8.45f_c. \end{cases} \quad (3)$$

Note that linear interpolation will be used to determine the value of ψ under different pressure levels when coding the material models.

The cap function F_c is non-dimensional, and ranges between zero and unity. In Huang et al. (2021)'s concrete model, F_c is defined as

$$F_c(I_1, k) = \begin{cases} 1, & I_1 < k, \\ 1 - \left(\frac{I_1 - k}{X(k) - k} \right)^2, & I_1 \geq k, \end{cases} \quad (4)$$

where I_1 is the first invariant of the stress tensor and k is an internal variable. $X(k)$ is a function of the internal variable k , which is formulated as:

$$X(k) = k + RF_r(k), \quad (5)$$

where R is a material constant. The relationship between $X(k)$ and k given in Eq. (5) determines the shape of the cap function. The function $F_r(k)$ in Eq. (5) is determined by substituting the pressure P in Eq. (2) with one-third of the internal variable k , which is then formulated as:

$$F_r(k) = \begin{cases} \frac{\sqrt{3}}{2\psi} (k/3 + T), & 0 \leq k < f_c, \\ \frac{\sqrt{3}}{3} \left(f_c + \frac{k/3 - f_c/3}{a_1 + a_2 k/3} \right), & k \geq f_c. \end{cases} \quad (6)$$

The ratio of the current meridian to the compressive meridian r' is defined as

$$r'(\theta, \psi) = \frac{2(1 - \psi^2) \cos \theta + (2\psi - 1) \sqrt{4(1 - \psi^2) \cos^2 \theta + 5\psi^2 - 4\psi}}{4(1 - \psi^2) \cos^2 \theta + (1 - 2\psi)^2}, \quad (7)$$

where θ denotes the Lode-angle.

Numerous investigations (Rossi, 1991) have revealed that under high strain-rate conditions, concrete material has much higher strength than that under quasi-static loadings. One cause of the strain-rate effect is associated with the free water in the capillary pores of the concrete. Due to the presence of free water, opposed viscous forces will be generated to delay or prevent the propagation of the microcracks and, at the macroscopic level, the material strength and stiffness increase (Huang et al., 2020). To account for the strain-rate effect, the radial enhancement approach is adopted, with the failure function Y enhanced as:

$$Y = r_{\text{DIF}}^2 \cdot Y(P/r_{\text{DIF}}), \quad (8)$$

where r_{DIF} represents the ratio of dynamic strength to static strength and DIF is the dynamic increase factor.

As for the relationship between r_{DIF} and strain rate, Huang et al. (2020) have proposed a concise semi-empirical formula with three material parameters:

$$r_{\text{DIF}} = 1.0 + \alpha e^{\beta(\log(\dot{\epsilon}/\dot{\epsilon}_0) - \chi)}, \quad (9)$$

where $\dot{\epsilon}$ is the strain rate and $\dot{\epsilon}_0 = 1 \text{ s}^{-1}$ is the reference strain rate. α , β , and χ are material parameters used to match with the test data. For concrete materials, the suggested values are $\alpha = 0.7$, $\beta = 0.45$, and $\chi = 1.7$. Because of the lack of test data, and to avoid overestimation, a constant value of 3.0 is set for strain rates exceeding $1 \times 10^4 \text{ s}^{-1}$. Only the strain-rate effect for compression is considered here. That is because the strain-rate effect for tension is naturally considered in the Taylor-Chen-Kuszmaul (TCK) model (Taylor et al., 1986) which has been completely incorporated into Huang et al. (2021)'s concrete model.

In addition, one may find that the defined plastic model is mainly dependent on the compressive strength f_c of the concrete material. In this way, the performance of the proposed model in predicting the mechanical behaviors in compression is highly dependent on f_c . Thus, f_c of the concrete material should be well calibrated.

2.2 Damage model

The major contribution of Huang et al. (2021)'s concrete model is the establishment of three damage mechanisms of rock-like materials, which are hydrostatic damage due to pore collapse, shear damage due to shear-induced microcracking, and tensile damage due to tensile microcracking. In this section, the three damage mechanisms will be briefly introduced.

Hydrostatic damage is proposed to account for the degradation of material properties due to pore collapse. This has been neglected in most of the other existing material models. The hydrostatic damage for concrete materials can be attributed to two factors. Firstly, concrete is typically a heterogeneous material. Unlike in some homogeneous materials, such as metals, stress concentrations and strain localizations will occur in concrete even under purely hydrostatic loading. As a result, the material can be damaged. Secondly, concrete is a porous material. Pores will be collapsed under high pressure, accompanied by a great

loss of cohesive strength—as pointed out in (Holmquist et al., 1993; Cui et al., 2017). Considering these two aspects, the hydrostatic damage in Huang et al. (2021)'s concrete model is formulated based on the irreversible plastic volumetric strain (plastic compaction). In a cap model, the following isotropic hardening rule is commonly used to update the internal variable k and to calculate the irreversible plastic volumetric strain:

$$\varepsilon_v^p = W \left(1 - e^{-D_1(X(k)-X_0) - D_2(X(k)-X_0)^2} \right), \quad (10)$$

where ε_v^p is the current plastic volumetric strain caused exclusively by pore collapse based on the current pressure level. W is the maximum plastic volumetric strain that is generally approximate to the initial porosity of the material. ε_v^p will be equal to W when all the pores have collapsed. X_0 corresponds to the initial I_1 , beyond which pores start to collapse. D_1 and D_2 are shape parameters, which should be determined by the hydrostatic compression test data. Then the hydrostatic damage D_c is proposed as:

$$D_c = \frac{\varepsilon_{v,\max}^p - \varepsilon_v^p}{W}, \quad (11)$$

where $\varepsilon_{v,\max}^p$ is the maximum plastic volumetric strain reached and depends on the maximum pressure level that the material has experienced.

As opposed to plastic compaction due to pore collapse, the shear will cause plastic dilatation to overcome the incompatibilities on the microcrack surfaces. In Huang et al. (2021)'s concrete model, the shear damage is formulated based on the growth of the plastic dilatation. To formulate the shear damage, a modified equivalent plastic volumetric strain λ is proposed as a function of the plastic dilatation, and is represented by:

$$\lambda = \sum \frac{d\varepsilon_v^p}{\zeta_1 (T/f_c + P/f_c)^{\zeta_2}}, \quad (12)$$

where $d\varepsilon_v^p = \sqrt{d\varepsilon_v^{pd} d\varepsilon_v^{pd}}$ is the effective plastic volumetric strain and $d\varepsilon_v^{pd}$ is the plastic dilatation increment which can be determined by the volumetric form of the flow rule. ζ_1 and ζ_2 are two material parameters related to shear damage evolution. Then, the shear damage D_s is defined as

$$D_s = \frac{\lambda}{\lambda + 1}. \quad (13)$$

To describe the tensile behavior of concrete, the TCK continuum damage model (Taylor et al., 1986) has been completely incorporated into Huang et al. (2021)'s concrete model. In the TCK model, the tensile damage is formulated based on the crack density C_d , which is formulated based on the current pressure level and defined as

$$C_d = \frac{5}{2} \frac{k_t}{(3K)^m} \left(\frac{K_{IC}}{\rho C} \right)^2 P^m \dot{\varepsilon}_v^{-2}, \quad (14)$$

where k_t and m are material constants. K is the bulk modulus. K_{IC} is the fracture toughness of the material. ρ is the mass density and C is the uniaxial wave speed. $\dot{\varepsilon}_v$ is the volumetric strain rate depending on which the strain-rate effect in tension is considered. Then, the tensile damage D_t is formulated as a function of C_d , as follows:

$$D_t = \frac{16}{9} \left(\frac{1 - \bar{\nu}^2}{1 - 2\bar{\nu}} \right) C_d, \quad (15)$$

where $\bar{\nu}$ is the degraded Poisson's ratio.

A core task in establishing different damage mechanisms is to identify their borders so that the established damage mechanisms will not intersect each other. In the present study, three damage mechanisms are considered, with the first two (hydrostatic damage and shear damage) related to stress states in compression, and the third one (tensile damage) associated with stress states in tension. In the computational codes, pressure is used to distinguish the stress states with $P > 0$ for compression and $P < 0$ for tension. Hence, the tensile damage can be easily distinguished, which will not intersect those in compression. Further, as discussed above, the hydrostatic damage and shear damage are generated by different physical mechanisms and accumulated exclusively with the corresponding plastic deformation, and hence they will not intersect each other. In this way, the three damage mechanisms are mutually independent and will not intersect each other.

In this study, the way the damage index degrades the stress tensor is different from that in the original Huang et al. (2021)'s concrete model. A total damage

D_{tot} is proposed based on the hydrostatic damage D_c , shear damage D_s , and tensile damage D_t , and is formulated as:

$$D_{\text{tot}} = \begin{cases} 1 - (1 - D_t)(1 - D_s)(1 - D_c), & P < 0, \\ 1 - (1 - D_s)(1 - s_c D_c), & P \geq 0, \end{cases} \quad (16)$$

where s_c is a material parameter. D_{tot} has different forms for tension with pressure $P < 0$ and for compression with pressure $P \geq 0$. For tension, previous study (Batzle et al., 1980) has shown that previous damage in compression will weaken the subsequent tensile behavior. Therefore, through the definitions of D_{tot} in Eq. (16), D_t is ‘strengthened’ by D_s and D_c . For instance, imagine that the concrete experiences compressive loadings firstly with $D_s=0.5$ and $D_c=0$ or $D_c=0.5$ and $D_s=0$, and then after that the concrete suffers from tensile loadings with $D_t=0.5$. The total damage D_{tot} based on Eq. (16) will be 0.75, which is higher than $D_t=0.5$ and thus can yield weaker tensile behavior. For compression, D_t is absent which means that the previous tensile damage will not affect the subsequent compressive behavior. It is mainly due to the microcrack closure effect (Batzle et al., 1980; Zhu and Arson, 2014), which is represented by the tensile microcracks that can be reclosed upon load reversal; consequently, the degraded compressive strength and modulus can be recovered. On the other hand, hydrostatic damage can influence the compressive behaviors. In addition, based on the experiments (Cui et al., 2017) and our previous study (Huang et al., 2021), it is found that the influence of hydrostatic damage is more severe on the tensile behavior compared with the compressive one. This accounts for the existence of the material parameter s_c in Eq. (16) for compression. Based on experiments (Cui et al., 2017) and our previous study (Huang et al., 2021), $s_c=0.6$ is suggested and will be used in this study.

Finally, the stress tensor will be degraded by the total damage through:

$$\boldsymbol{\sigma}^{n+1} = \boldsymbol{\sigma}_p^{n+1}(1 - D_{\text{tot}}), \quad (17)$$

where $\boldsymbol{\sigma}^{n+1}$ is the updated stress tensor that will be returned to the host code and $\boldsymbol{\sigma}_p^{n+1}$ is the stress tensor updated from the plastic model for compression or the elastic model for tension.

3 Comparison with ballistic experiments

A set of well-designed penetration and perforation experiments into plain concrete slabs with the projectile data recorded was presented in (Forquin et al., 2015). Damage profiles of the concrete targets were also given based on topographic analysis. In this study, a numerical study based on these ballistic experiments will be carried out. Before the numerical study, the adopted Huang et al. (2021)’s concrete model will be sufficiently validated in this section by comparisons with the experimental results in (Forquin et al., 2015). Approaches to calibrate the required parameters are given. Element erosion criteria are introduced into Huang et al. (2021)’s concrete model. Influences of the element erosion criterion and mesh size of the concrete target are presented.

3.1 Parameter calibration

There are in total 17 material parameters required in Huang et al. (2021)’s concrete model. These parameters can be classified into four categories. Approaches for determining these parameters will be discussed here.

The first category contains the common material parameters including the mass density ρ , Young’s modulus E , Poisson’s ratio ν , compressive strength f_c , and tensile strength T . These parameters can be obtained relatively easily. Table 1 summarizes these parameters that will be used in the numerical simulations. ρ and E are acquired from the experiments in (Forquin et al., 2015), while f_c and T are empirically determined in (Kong et al., 2018) based on Young’s modulus. A commonly used value of ν , i.e., 0.2, is adopted for the concrete.

The second category contains the shear behavior related parameters, including strength parameters a_1 and a_2 in the fracture function, and shear damage evolution parameters ζ_1 and ζ_2 . a_1 and a_2 should be determined by matching with the triaxial compression test data. A set of triaxial compression test data for concrete (Xie et al., 1996; Hou, 2006; Xiong, 2009) with similar material properties to that used in the ballistic experiments of Forquin et al. (2015) has been collected, as shown in Fig. 2a. With these test data, a_1 and a_2 have been calibrated to be $a_1=0.5876$ and $a_2=0.025/f_c$. ζ_1 and ζ_2 can be determined by the softening portion of the strain–stress curves in an unconfined

uniaxial compression test. The suggested values for ζ_1 and ζ_2 are 0.02 and 1.5, respectively.

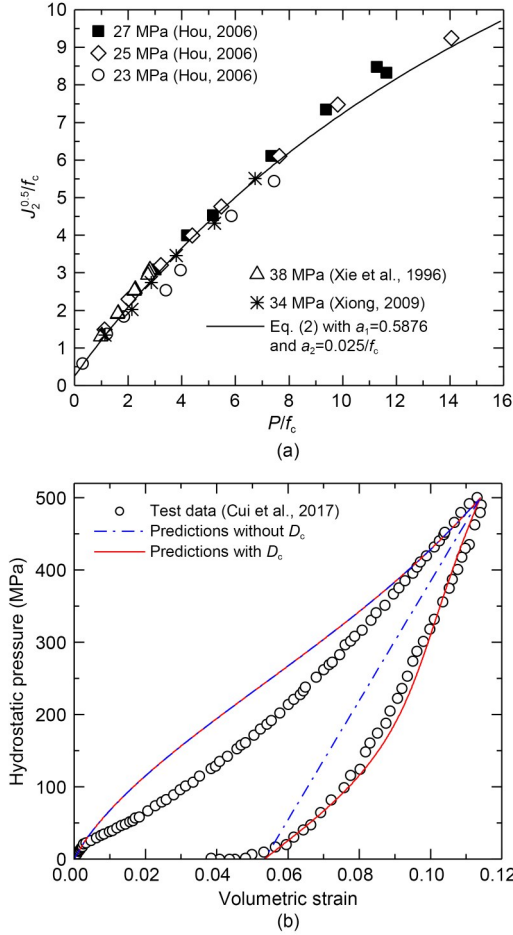


Fig. 2 Behaviors of concrete under high confining pressure and fitting curves for Huang et al. (2021)'s model: (a) shear behaviors; (b) volumetric behaviors

The third category contains the volumetric behavior related parameters, including the hardening parameters W , R , X_0 , D_1 , and D_2 . These parameters should be determined by the hydrostatic compression test data. A set of hydrostatic data for concrete is available in (Forquin et al., 2015); however, it lacks the unloading stage that is important to demonstrate the hydrostatic damage mechanism proposed in Huang et al. (2021)'s concrete model. In view of this, the volumetric strain–pressure curve for concrete with the unloading process from experiments (Cui et al., 2017) is adopted to calibrate these parameters. By matching with the test data, the hardening parameters are calibrated with $W=0.06$, $R=6$, $X_0=102$ MPa, $D_1=1.22 \times 10^{-10}$ Pa⁻¹, and $D_2=1.00 \times 10^{-18}$ Pa⁻². The predicted

volumetric strain–pressure curves by Huang et al. (2021)'s concrete model, with and without consideration of D_c , together with test data (Cui et al., 2017) are depicted in Fig. 2b. Differences exist in the unloading process. By inspection of Fig. 2b, one may find that predictions with D_c can reflect the bulk modulus degradations during the unloading process, and are very consistent with the test data. However, predictions without D_c are linear and parallel to the initial loading stage with no degradations of the bulk modulus, which is inconsistent with the test data. This phenomenon demonstrates the need to consider the hydrostatic damage due to pore collapse.

The fourth category contains the tensile behavior related parameters, including material constants k_t and m , and the fracture toughness K_{IC} . Approaches to determine these parameters have been fully discussed in the TCK model (Taylor et al., 1986). The widely used parameters for concrete, as suggested in (Huang et al., 2005; Wang et al., 2007), are adopted here, with $k_t=5.753 \times 10^{21}$ m⁻³, $m=6$, and $K_{IC}=2.74 \times 10^6$ Pa·m^{0.5}.

All the determined or suggested parameters for Huang et al. (2021)'s concrete model are summarized in Table 1 and will be used in this study.

Table 1 Material parameters of the current model for concrete

Category	Parameter	Description
Common parameter	ρ (kg/m ³)	2390
	E (GPa)	42
	ν	0.2
	f_c (MPa)	35
	T (MPa)	3.2
	Shear parameter	a_1
a_2		$0.025/f_c$
ζ_1		0.02
ζ_2		1.5
Volumetric parameter		W
	R	6
	X_0 (MPa)	102
	D_1 (Pa ⁻¹)	1.22×10^{-10}
	D_2 (Pa ⁻²)	1.00×10^{-18}
Tensile parameter	k_t (m ⁻³)	5.753×10^{21}
	m	6
	K_{IC} (Pa·m ^{0.5})	2.74×10^6

3.2 Numerical model

In the penetration and perforation experiments presented in (Forquin et al., 2015), a steel projectile

with filler was launched into a cylindrical unreinforced concrete target. The ogive-nosed steel projectile was 52 mm in diameter and 300 mm in length, with a mass of 2.4 kg. For the penetration case, the concrete target was 800 mm in thickness and was impacted by the projectile with an initial velocity of 347 m/s. For the perforation case, the concrete target was 300 mm in thickness and was impacted by the projectile with an initial velocity of 333 m/s. In both cases, the concrete targets were 800 mm in diameter. The cylindrical concrete targets were surrounded by steel rings to constrain the radial displacement. In the present study, both the penetration and perforation cases are simulated. Fig. 3 presents the numerical models. Considering the symmetry of the experiments, only 1/4 of the concrete target, the steel projectile, and the steel rings are simulated to save the computational time. Symmetric boundary conditions are applied on the symmetric planes. The steel projectile and the steel rings are taken as rigid bodies. The penalty method available in LS-DYNA is implemented here to define the contact behaviors. Specifically, the keyword ‘contact erosion surface to surface’, is employed to describe the interaction between the concrete target and the steel projectile, as well as between the concrete target and the steel rings.

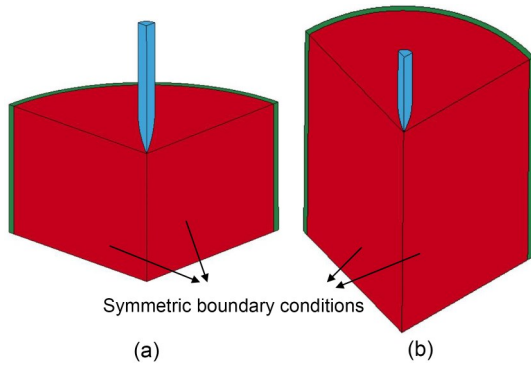


Fig. 3 Numerical models of the ballistic experiments: (a) 300 mm thin concrete target perforated by a projectile at 333 m/s; (b) 800 mm thick concrete target penetrated by a projectile at 347 m/s

3.3 Influence of friction, element erosion, and mesh size

3.3.1 Frictional effect

Studies (Forquin et al., 2015; Zhao and Wen, 2018) have pointed out that friction should be considered when conducting impacting simulations. The

frictional effect can be introduced easily through the contact algorithm available in LS-DYNA. The equation to describe the friction is formulated as:

$$\mu_c = F_D + (F_S - F_D)e^{-\gamma \cdot V_{rel}}, \quad (18)$$

where μ_c is the coefficient of friction. F_D is the dynamic coefficient of friction and F_S is the static coefficient of friction. V_{rel} is the relative velocity of the surface in contact and γ is the exponential decay coefficient. The values of these coefficients based on research (Forquin et al., 2015; Zhao and Wen, 2018) are used, i.e., $F_D=0.05$, $F_S=0.5$, and $\gamma=0.07$.

3.3.2 Element erosion criterion

Within the finite element method, the element erosion criterion is critical and is used not only to trigger the initiation and growth of cracks but also to delete the distorted elements. Otherwise, the failure of concrete structures subjected to dynamic loadings always involves large strain which results in the mesh entanglement and distortion that can prematurely terminate the numerical analysis. In the original Huang et al. (2021)’s concrete model, the element erosion criterion was absent since no numerical simulations at a structural level were involved. In this study, the element erosion criterion will be introduced into Huang et al. (2021)’s concrete model as follows.

For compression with pressure $P \geq 0$, the element will be deleted when a selected function λ_i is larger than a user-defined value λ_c^f . In this study, the selected function λ_c is defined based on the effective volumetric strain, as follows:

$$\lambda_c = \sum \sqrt{d\epsilon_v^{pd} d\epsilon_v^{pd}}. \quad (19)$$

By the definition of Eq. (19), the element will be deleted with the presence of severe volumetric deformation. The user-defined value λ_c^f should be determined by comparisons with the experimental data. For tension with pressure $P < 0$, the element will be deleted when D_i is larger than 0.5. This element erosion criterion for the TCK model has been examined in many previous studies (Huang et al., 2005; Wang et al., 2007), where reasonable predictions can be obtained. Hence, this element erosion criterion for tension will also be adopted here.

Test data of the projectile velocity–time histories for the perforation case are used to determine the λ_c^f for the element erosion criterion in compression. Fig. 4 presents the predicted projectile velocity–time histories with $\lambda_c^f=0.20, 0.26,$ and $0.30,$ together with the test data. It is found that different user-defined values of λ_c^f can strongly affect the projectile velocity–time histories. With the increase of $\lambda_c^f,$ the residual velocity of the projectile decreases. On the whole, the predictions with $\lambda_c^f=0.26$ are more consistent with the test data. Hence, hereinafter, $\lambda_c^f=0.26$ and $D_t=0.5$ (Huang et al., 2005; Wang et al., 2007) will be adopted to delete the distorted elements.

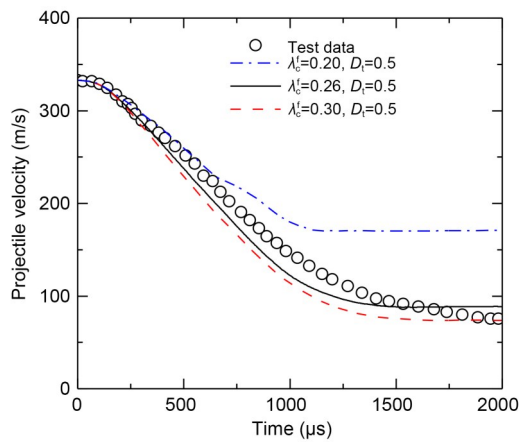


Fig. 4 Influence of element erosion criterion on the projectile velocity–time histories for a 300 mm concrete target perforated by a steel projectile at 333 m/s

3.3.3 Mesh size effect

The influence of mesh size for the concrete target is evaluated. The predicted projectile velocity–time histories for the perforation case with mesh sizes of 2.5, 4.0, and 6.0 mm are presented in Fig. 5. Very similar results are obtained for the three mesh sizes and, with the increase of the mesh size, the residual velocity of the projectile decreases slightly. For a sake of balance between efficiency and accuracy, a mesh size of 4.0 mm for the concrete target will be used.

3.4 Comparison and validation

With the parameters summarized in Table 1, the numerical models illustrated in Fig. 3, the element erosion criterion discussed in Section 3.3.2, and the mesh size of 4.0 mm for the concrete target determined in Section 3.3.3, numerical simulations for both

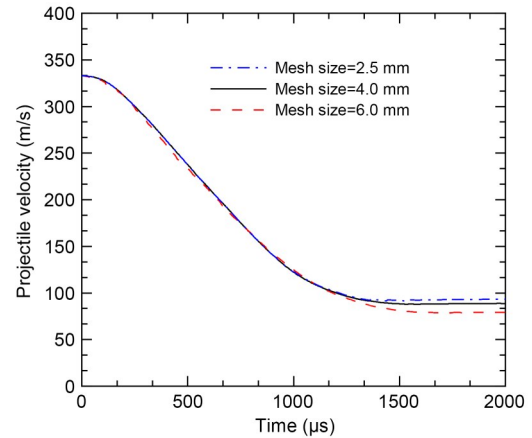


Fig. 5 Influence of the mesh size for the concrete target on the projectile velocity–time histories for a 300 mm concrete target perforated by a steel projectile at 333 m/s

the perforation and penetration cases are carried out. Figs. 6 and 7 present comparisons between numerical predictions and experimental results for failures in concrete targets after impacts for the perforation and penetration cases, respectively. For the perforation case with a 300 mm thin concrete target impacted by a projectile at 333 m/s, as shown in Fig. 6, the three typical failure modes can be clearly observed, i.e., cratering on the front face, tunneling in the center, and scabbing on the rear face. The numerically predicted failure patterns shown in Fig. 6b are reasonably consistent with those obtained experimentally and illustrated in Fig. 6c. For the penetration case with an 800 mm thick concrete target impacted by a projectile at 347 m/s, as shown in Fig. 7, the scabbing on the rear face is absent since the projectile will not perforate the concrete target. However, the cratering on the front face and the tunneling region can still be clearly seen. Again, the failure patterns obtained numerically and experimentally, shown in Figs. 7b and 7c respectively, agree well.

Comparisons between numerical predictions and experimental data for the projectile data for both the perforation and penetration cases are presented in Fig. 8. One may find that the numerically predicted projectile data including the acceleration–time histories, the velocity–time histories, and the penetration depth–time histories are very consistent with the corresponding experimental data. Furthermore, by inspection of Figs. 6 and 8a for the perforation case, there are three obvious stages in the projectile acceleration–time histories, which correspond to the three failure modes shown in Fig. 6:

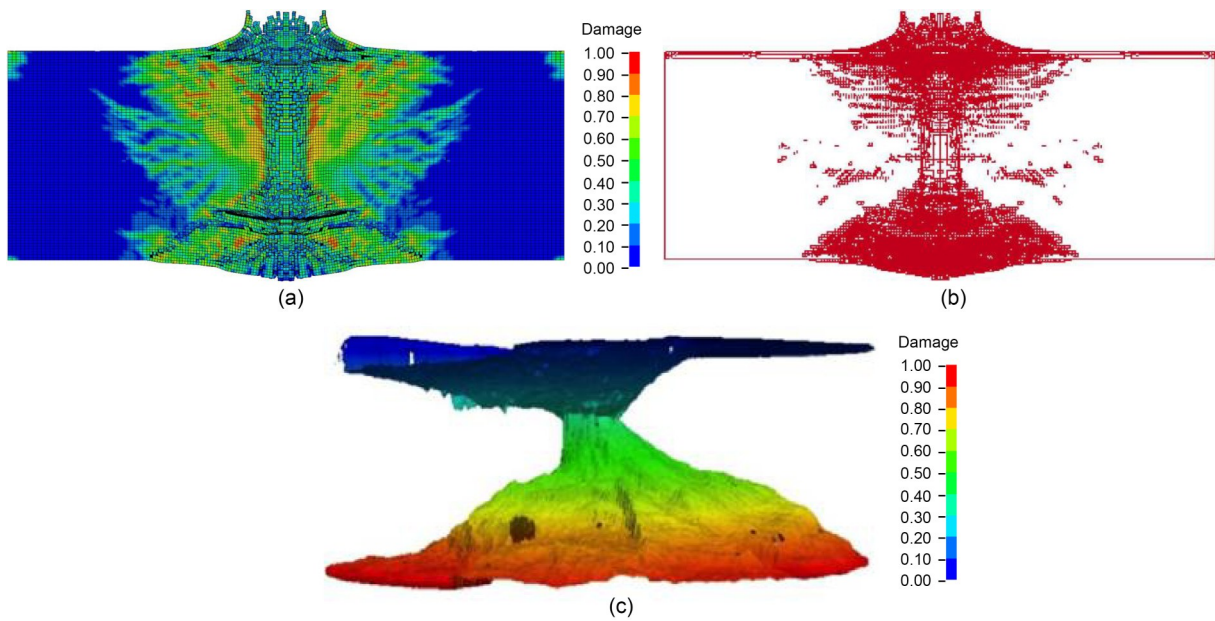


Fig. 6 Comparisons between numerical predictions and experimental results for the concrete targets after impacts for the perforation case: (a) numerically predicted damage profiles (section view); (b) numerically predicted failure patterns (section view); (c) experimentally obtained failure patterns (topographic analysis). References to color refer to the online version of this figure

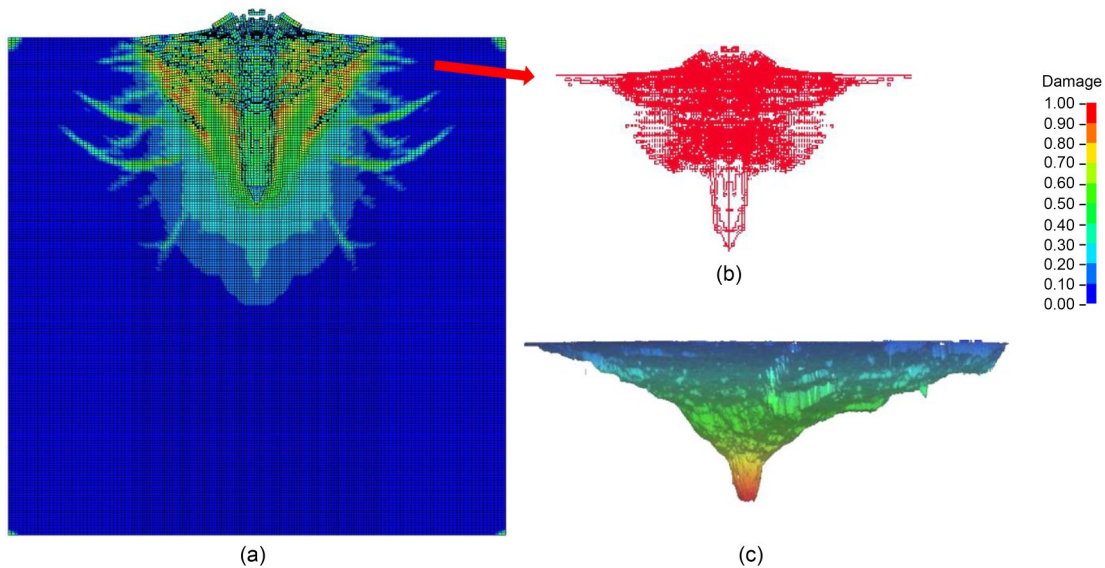


Fig. 7 Comparisons between numerical predictions and experimental results for the concrete targets after impacts for the penetration case: (a) numerically predicted damage profiles (section view); (b) numerically predicted failure patterns (section view); (c) experimentally obtained failure patterns (topographic analysis). References to color refer to the online version of this figure

(1) The first stage (entrance phase). This stage is from the start to 300 μ s. In this stage, the projectile acceleration increases linearly. This stage generally corresponds to the entrance phase of the projectile; the typical failure mode, i.e., cratering on the front face of the concrete target, belongs to this stage.

(2) The second stage (tunneling in the center). This stage is from 300 to 750 μ s. In this stage, it is observed that the projectile acceleration is almost constant. Tunneling in the center of the concrete target belongs to this stage and the size of the tunnel is approximately the projectile diameter.

(3) The third stage (exit phase). After $750 \mu\text{s}$ comes the third stage. In this stage, the projectile acceleration decreases almost linearly. This stage is generally accompanied by the exit phase of the projectile; the typical failure mode, i.e., scabbing on the rear face of the concrete target, belongs to this stage.

Very similar results can be observed for the penetration case except for the absence of the third stage (exit phase). As shown in Fig. 8c, there are two stages in the acceleration–time histories of the projectile. The first stage corresponds to the entrance phase of the projectile, from the start to $300 \mu\text{s}$, and the acceleration of the projectile increases linearly. Cratering on the front face of the concrete target can also be observed in this stage, as shown in Fig. 7. After $300 \mu\text{s}$ comes the second stage (around $300\text{--}1300 \mu\text{s}$). Again, in this stage, the projectile acceleration is almost

constant. Tunneling with size approximate to the projectile diameter can be observed.

4 Numerical study

The good performance of Huang et al. (2021)'s concrete model demonstrated in the ballistic simulations above is the solid foundation of the numerical study performed in this section. The major two points and especially the detailed four aspects discussed previously will be investigated. The numerical study is arranged by changing the mechanical behaviors of the target in one aspect while those in the other aspects remain unchanged. In this way, the individual influence of the tensile, volumetric, and shear behaviors of the target on its ballistic performance can be accessed. Some interesting findings are obtained.

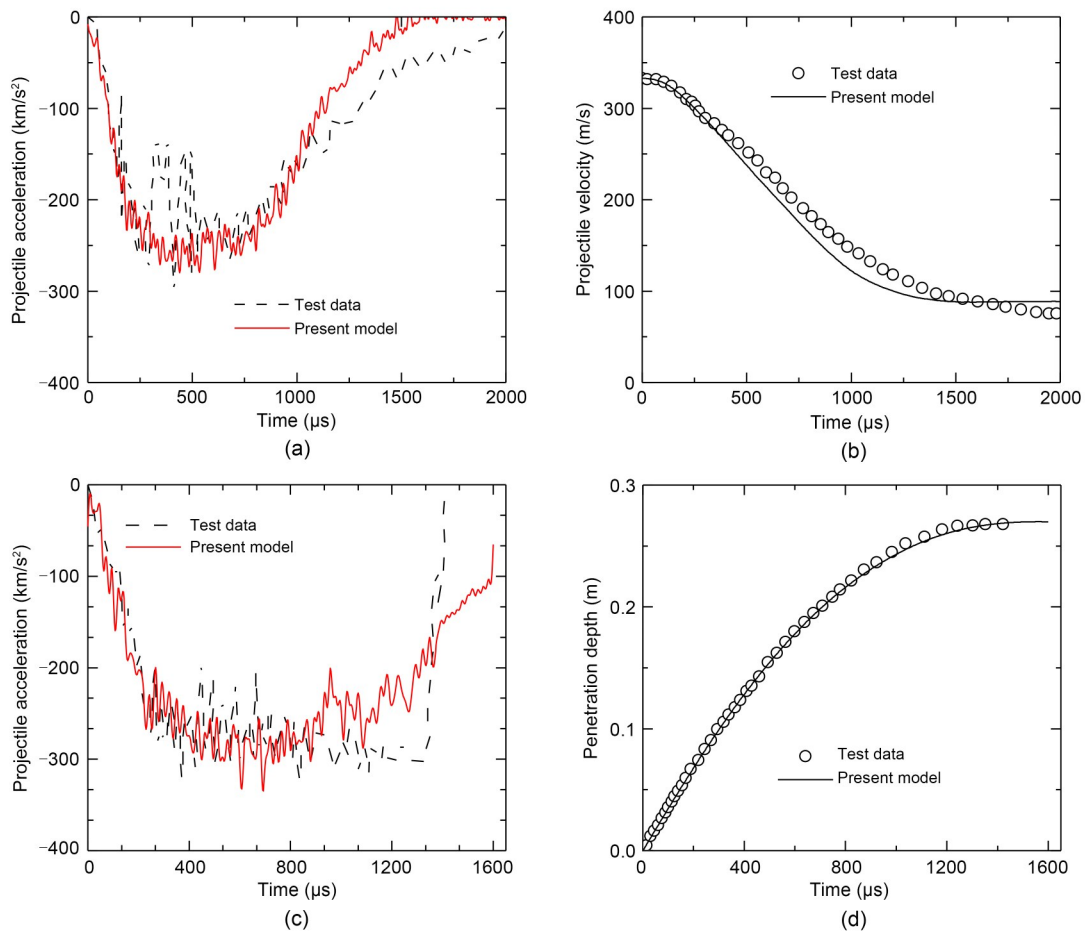


Fig. 8 Comparisons of projectile data between numerical predictions and experimental data: projectile acceleration–time histories (a) and projectile velocity–time histories (b) for the perforation case; projectile acceleration–time histories (c) and penetration depth–time histories (d) for the penetration case

4.1 Influence of tensile behavior

In Huang et al. (2021)'s concrete model, the tensile behavior is completely described by the TCK model. Tensile behaviors including the strain-rate effect and the tensile damage evolution are governed by parameters k_t , m , and K_{IC} . Changing some of them, the concrete will show different tensile behaviors no matter which of them is changed. To investigate the influence of the tensile behavior, five different tensile parameter schemes are arranged, as listed in Table 2. In the arrangement, parameters m and K_{IC} are maintained, with k_t ranging between 5.753×10^{19} and 5.753×10^{23} (one may also choose to change one of the other parameters and maintain the other two). A larger k_t yields weaker tensile behaviors represented by lower tensile strengths and higher damage growth rates. Considering this, the five tensile parameter schemes in Table 2 are marked with 'Low', 'Med low', 'Normal', 'Med high', and 'High', based on the tensile behaviors behind the schemes. One may thus gain an insight into the influence of the five parameter schemes through the predicted strain–stress relations of an unconfined uniaxial tension test with a strain rate of 10 s^{-1} shown in Fig. 9. Then, with the five tensile parameter schemes, numerical simulations for both the perforation and penetration cases are conducted. It is worth noting that, except for the tensile parameters stated in Table 2, all the other parameters used in this section are the same as those summarized in Table 1.

Table 2 Five different tensile parameter schemes for investigating the influence of concrete tensile behavior on its failure modes and penetration resistance against impacts

Scheme	$k_t \text{ (m}^{-3}\text{)}$	m	$K_{IC} \text{ (Pa} \cdot \text{m}^{0.5}\text{)}$
Low	5.753×10^{23}	6	2.74×10^6
Med low	5.753×10^{22}	6	2.74×10^6
Normal	5.753×10^{21}	6	2.74×10^6
Med high	5.753×10^{20}	6	2.74×10^6
High	5.753×10^{19}	6	2.74×10^6

With regard to the target resistance, the projectile data for both the perforation and penetration predicted with tensile parameter schemes marked with 'Low', 'Normal', and 'High' are presented in Fig. 10. For the perforation case, by inspection of Fig. 10a, it is found that before $750 \mu\text{s}$, the projectile acceleration–time histories of the three parameter schemes are almost

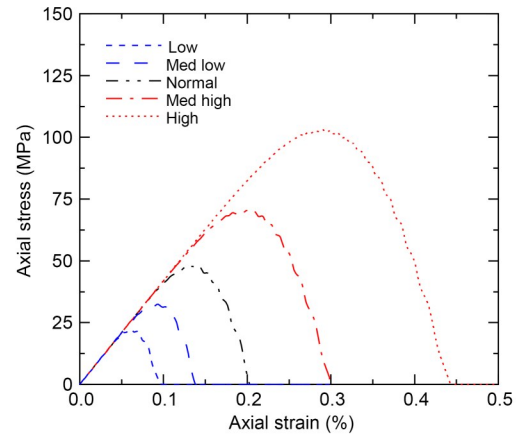


Fig. 9 Predicted strain–stress relations of an unconfined uniaxial tension test for five different parameter schemes as summarized in Table 2

the same. However, after $750 \mu\text{s}$, deviations appear. With the tensile parameter schemes varying from 'Low' to 'Normal', and to 'High', the projectile acceleration shows a great increase. Together with the discussion in Section 3.4, one may conclude that for the target resistance, tensile behaviors show very limited influences on the first cratering stage and the second tunneling stage. However, for the third scabbing stage, tensile behaviors play a key role. The projectile velocity–time histories illustrated in Fig. 10b show a similar tendency with differences appearing after $750 \mu\text{s}$. Furthermore, with the tensile parameter schemes varying from 'Low' to 'High', the residual velocities of the projectile decrease dramatically, which indicates that tensile behaviors play an important role in accounting for the target resistance for a perforation case. The detailed residual velocities of the projectile can also be found in Table 3, where quantitative comparisons of the residual velocity, penetration depth, cratering size, and scabbing size are presented for the five tensile parameter schemes.

For the penetration case, as shown in Fig. 10c, the projectile acceleration–time histories of the three tensile parameter schemes are almost identical. It is because the penetration case only comprises the first two stages, where tensile behaviors are not important, while the third stage where tensile behaviors play a major role is absent. Likewise, the penetration depths shown in Fig. 10d and summarized in Table 3 for different tensile parameter schemes are very close. In this context, one may conclude that tensile behaviors have very limited influence on the target resistance

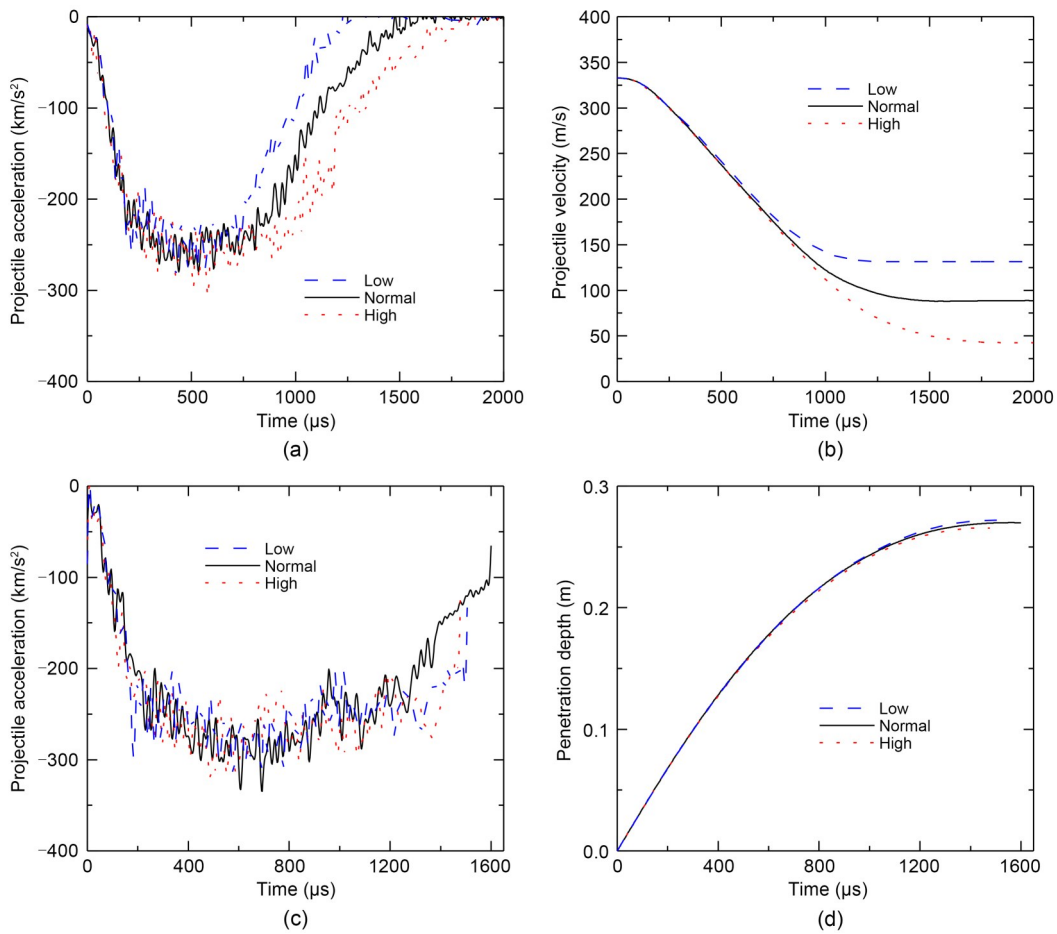


Fig. 10 Influence of concrete tensile behavior on the projectile data: projectile acceleration–time histories (a) and projectile velocity–time histories (b) for the perforation case; projectile acceleration–time histories (c) and penetration depth–time histories (d) for the penetration case

Table 3 Influence of concrete tensile behavior on its impact resistance and failure modes

Scheme	300 mm thin concrete targets perforated by 333 m/s projectile			800 mm thick concrete targets penetrated by 347 m/s projectile	
	Residual velocity (m/s)	Cratering size (mm)	Scabbing size (mm)	Penetration depth (mm)	Cratering size (mm)
Low	131.3 (+48.0%)	461.3 (+23.1%)	720.7 (+78.6%)	0.2719 (+0.7%)	417.4 (+4.3%)
Med low	117.1 (+32.0%)	396.4 (+5.8%)	518.9 (+28.6%)	0.2723 (+0.9%)	446.1 (+11.4%)
Normal (baseline)	88.7	374.8	403.6	0.2699	400.3
Med high	87.9 (−0.9%)	367.1 (−2.1%)	381.7 (−5.4%)	0.2694 (−0.2%)	389.4 (−2.7%)
High	42.5 (−52.1%)	266.7 (−28.8%)	302.7 (−25.0%)	0.2655 (−1.6%)	382.3 (−4.5%)

Values given in brackets refer to the differences relative to the ‘Normal’ scheme

for a penetration case. This conclusion is in common with most of the existing analytical models and empirical formulae where the influence of tensile behaviors is commonly ignored when formulating the target resistance and penetration depth (Rosenberg and Dekel, 2010; Kong et al., 2017a).

As for the influence of tensile behaviors on the failure modes of the target, the failure patterns of the

target predicted associated with the five tensile parameter schemes are illustrated in Fig. 11. It is found that both the cratering on the front face and the scabbing on the rear face are strongly affected by the tensile behaviors. By inspection of Fig. 11 and Table 3, it is found that in general, stronger tensile behaviors of the target yield smaller sizes of both the cratering and the scabbing.

4.2 Influence of volumetric behavior

In Huang et al. (2021)'s concrete model, the volumetric behavior of the concrete involves two aspects, i.e., compaction behaviors described by the pressure versus volumetric strain, and the hydrostatic damage due to pore collapse. Both aspects are governed by the isotropic hardening rule formulated in Eq. (10). The volumetric behavior is controlled by the following five parameters: W , R , X_0 , D_1 , and D_2 . Five volumetric parameter schemes are arranged, as listed in Table 4. In the arrangement, parameters W , R , X_0 , and D_1 are unchanged, with parameter D_2 ranging between 0.50×10^{-18} and 1.50×10^{-18} . A higher D_2 will produce lower compaction behaviors and higher hydrostatic damage growth rates. One may gain an insight into the influence of D_2 through the predicted pressure versus volumetric strain, and the growth of hydrostatic damage with pressure, which are shown in Fig. 12. Then, numerical simulations for both the perforation and penetration are carried out. Likewise, except for the volumetric parameters stated in Table 4, all the other parameters used in this section are the same as those listed in Table 1.

For the target resistance, the projectile data for both the perforation and penetration, with volumetric parameter schemes marked with 'Low', 'Normal', and 'High', are presented in Fig. 13. For the perforation case illustrated in Fig. 13a, it is found that the biggest difference appears in the second tunneling stage. With the volumetric parameter schemes varying from 'Low' to 'High', the nearly constant acceleration during the second tunneling stage increases from

Table 4 Five different volumetric parameter schemes for investigating the influence of concrete volumetric behavior on its failure modes and penetration resistance against impacts

Scheme	W	R	X_0 (MPa)	D_1 (Pa ⁻¹)	D_2 (Pa ⁻²)
Low	0.06	6	102	1.22×10^{-10}	1.50×10^{-18}
Med low	0.06	6	102	1.22×10^{-10}	1.25×10^{-18}
Normal	0.06	6	102	1.22×10^{-10}	1.00×10^{-18}
Med high	0.06	6	102	1.22×10^{-10}	0.75×10^{-18}
High	0.06	6	102	1.22×10^{-10}	0.50×10^{-18}

approximately -200 to -300 km/s². The first cratering stage coincides with each other except for the maximum acceleration values influenced by the second tunneling stage. The third scabbing stage is parallel and probably consistent with each other without the influences from the second tunneling stage. From this point of view, it is concluded that the volumetric behavior mainly affects the second tunneling stage and has very limited influence on the first cratering and third scabbing stages. Likewise, the projectile velocity–time curves, depicted in Fig. 13b, show differences after 300 μs that correspond to the second tunneling stage. In addition, with the volumetric parameter schemes varying from 'Low' to 'High', the residual velocities of the projectile decrease dramatically, which indicates that volumetric behaviors play a key role in accounting for the target resistance for a perforation case. The detailed residual velocities of the projectile can also be found in Table 5, where quantitative comparisons of the residual velocity, penetration depth, the cratering size, and the scabbing size are presented for the five volumetric parameter schemes.

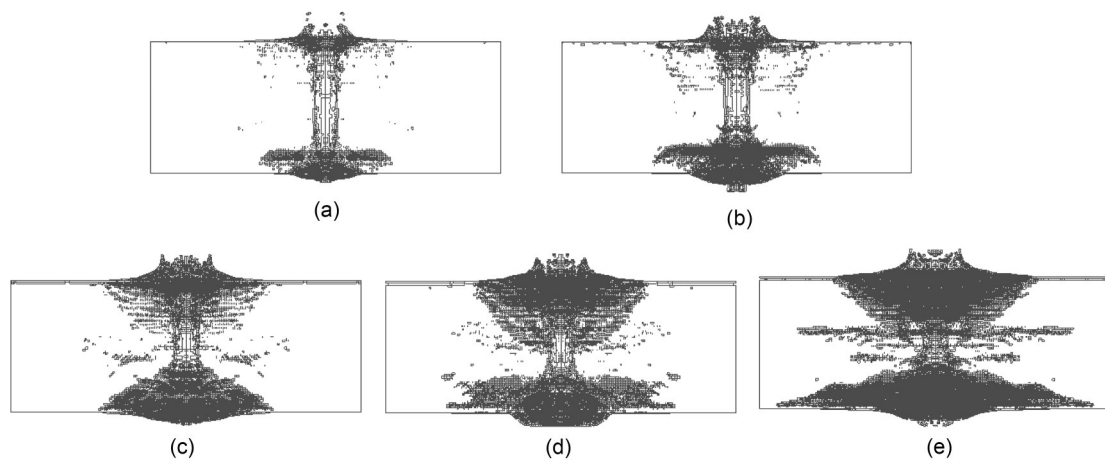


Fig. 11 Failure patterns of the concrete target after impacts for the perforation case predicted with five different tensile parameter schemes: (a) High; (b) Med high; (c) Normal; (d) Med low; (e) Low

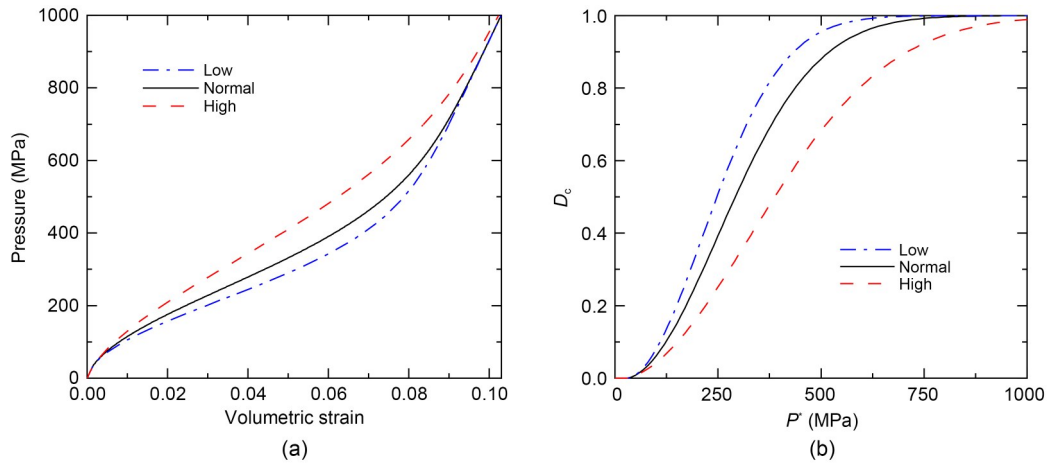


Fig. 12 Influence of D_2 on the volumetric behavior of concrete: (a) pressure versus volumetric strain; (b) growth of the hydrostatic damage with pressure. P^* represents the difference between the historical maximum pressure level and the current pressure level

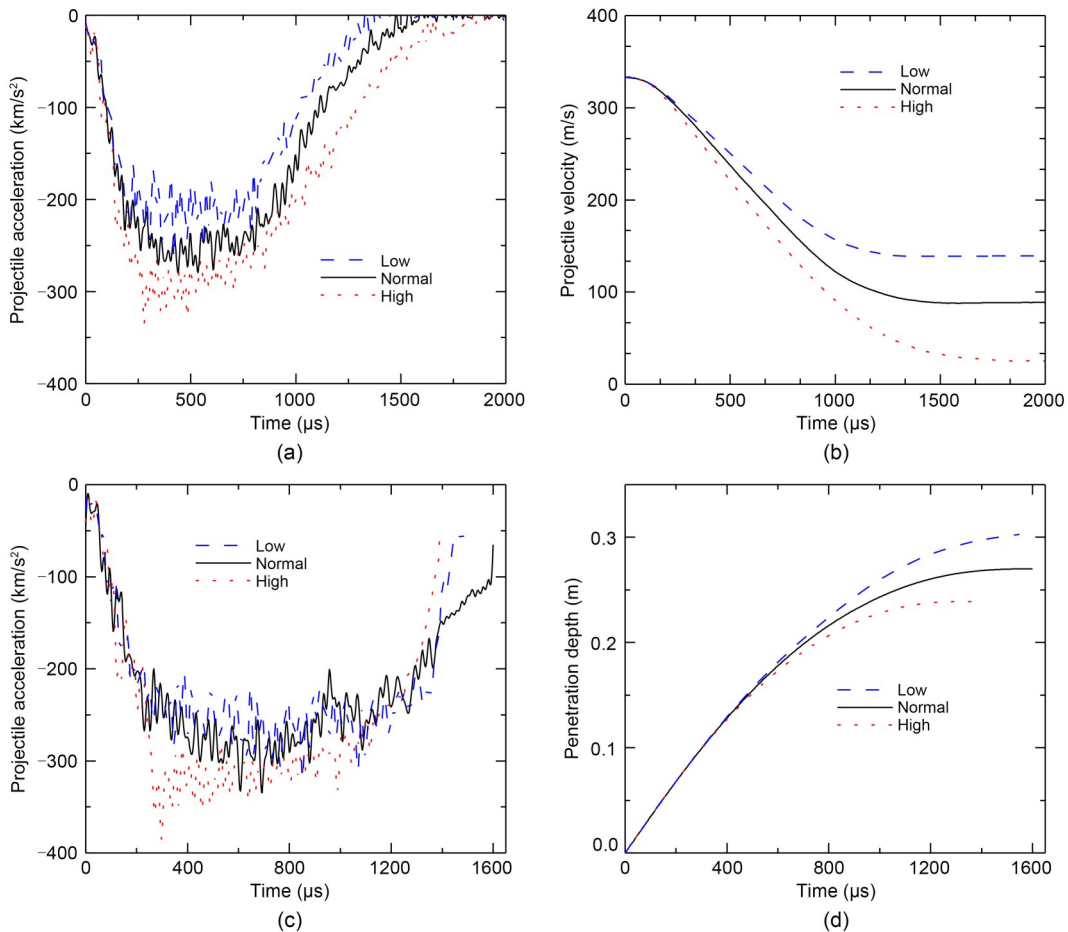


Fig. 13 Influence of concrete volumetric behavior on the projectile data: projectile acceleration–time histories (a) and projectile velocity–time histories (b) for the perforation case; projectile acceleration–time histories (c) and penetration depth–time histories (d) for the penetration case

For the penetration case illustrated in Fig. 13c, very similar results can be observed—except for the

third stage which is absent. Again, the biggest difference is in the second tunneling stage. Likewise, the

penetration depths shown in Fig. 13c and Table 5 are rather different. The stronger volumetric behavior can produce a much smaller penetration depth, which indicates that the volumetric behavior can significantly affect the target resistance. This conclusion supports most of the existing analytical models and empirical formulae where the relation between pressure and volumetric strain is involved in predicting the target resistance and penetration depth (Masri and Durban, 2005; Kong et al., 2017a).

Fig. 14 presents the hydrostatic damage due to pore collapse in the concrete target under perforation. It can be observed that the hydrostatic damage distributes all around the tunneling in the center of the concrete target, which is consistent with the discussion above that the concrete volumetric behavior mainly influences the second tunneling stage. In addition, one

may find that with the volumetric parameter schemes varying from ‘High’ to ‘Low’, the hydrostatic damage becomes more and more severe. It must be pointed out that damage due to pore collapse under high pressure has been reported in depth by experiments (Cui et al., 2017). However, this kind of damage mechanism has commonly been neglected in most of the other numerical studies.

As for the failure modes of the target, the results presented in Table 5 suggest that the volumetric behavior has very limited influence, supported by the very similar cratering sizes and scabbing sizes for the five different volumetric parameter schemes. This can also be concluded from the hydrostatic damage profiles presented in Fig. 14, where no hydrostatic damage can be observed on the front face or the rear face of the concrete target.

Table 5 Influence of concrete volumetric behavior on its impact resistance and failure modes

Scheme	300 mm thin concrete targets perforated by 333 m/s projectile			800 mm thick concrete targets penetrated by 347 m/s projectile	
	Residual velocity (m/s)	Cratering size (mm)	Scabbing size (mm)	Penetration depth (mm)	Cratering size (mm)
Low	139.2 (+56.9%)	387.0 (+3.3%)	393.1 (-2.6%)	0.3029 (+12.2%)	391.7 (-2.1%)
Med low	116.9 (+31.8%)	405.8 (+8.3%)	357.4 (-11.4%)	0.2833 (+5.0%)	403.7 (+0.8%)
Normal (baseline)	88.7	374.8	403.6	0.2699	400.3
Med high	67.1 (-24.4%)	430.4 (+14.8%)	410.8 (+1.8%)	0.2514 (-6.9%)	430.0 (+7.4%)
High	25.0 (-71.8%)	433.5 (+15.7%)	394.1 (-2.4%)	0.2384 (-11.7%)	436.1 (+8.9%)

Values given in brackets refer to the differences relative to the ‘Normal’ scheme

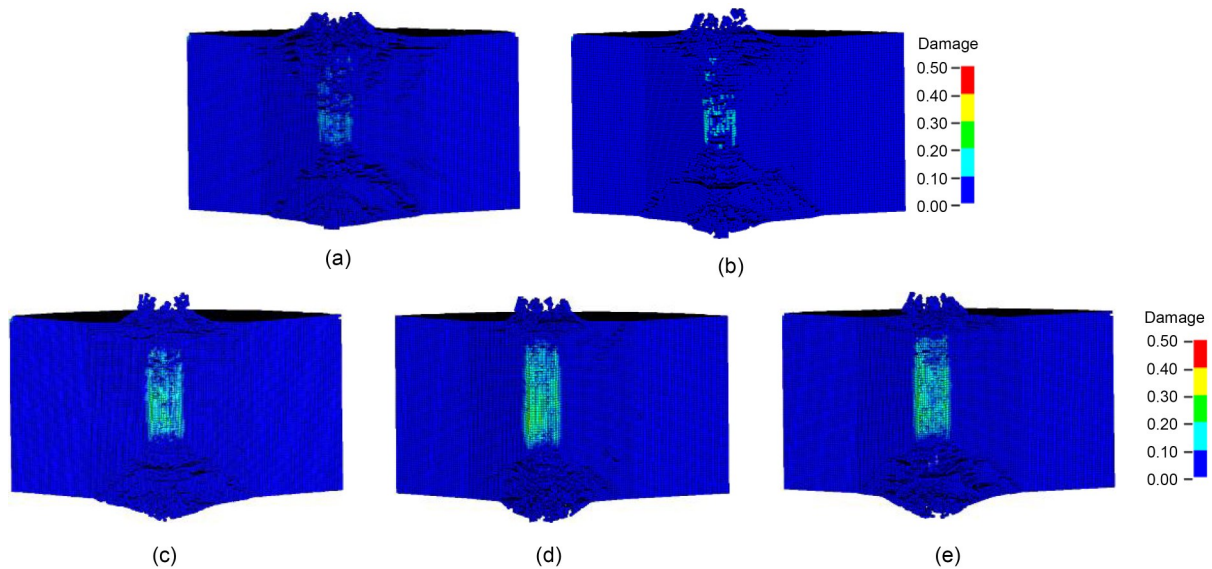


Fig. 14 Hydrostatic damage due to pore collapse in the concrete target for the perforation case with five different volumetric parameter schemes: (a) High; (b) Med high; (c) Normal; (d) Med low; (e) Low. References to color refer to the online version of this figure

4.3 Influence of shear behavior

In Huang et al. (2021)'s concrete model, the shear behavior relates to two aspects, i.e., shear strength versus pressure described by the fracture function in Eq. (2), and shear damage. Four parameters will influence the shear behavior, including strength parameters a_1 and a_2 , and shear damage parameters ζ_1 and ζ_2 . Likewise, five different shear parameter schemes are arranged to investigate the influence of shear behavior, as listed in Table 6. In the arrangement, parameters a_2 , ζ_1 , and ζ_2 are unchanged, with parameter a_1 ranging between 0.5000 and 0.8000. A larger a_1 will produce lower shear strengths and a higher shear damage growth rate. One may gain an insight into the influence of a_1 through the shear strength versus pressure, which is shown in Fig. 15. Then, numerical simulations for both the perforation and penetration are carried out. Again, except for the shear parameters stated in Table 6, all the other parameters used in this section are the same as those listed in Table 1.

The influence of the shear behavior on the target resistance is very similar to that of the volumetric behavior discussed above, with the projectile acceleration curves, as shown in Fig. 16, coinciding with each other in the first cratering stage, differing in the second tunneling stage, and being parallel to each other in the third scabbing stage (for the perforation case). Both the residual velocities and penetration depths show a significant decrease, with the shear behavior becoming stronger, which indicates the importance of the shear behavior in accounting for the target resistance. Detailed discussions are not repeated. However, it must be pointed out that these observations are again consistent with most of the existing analytical models

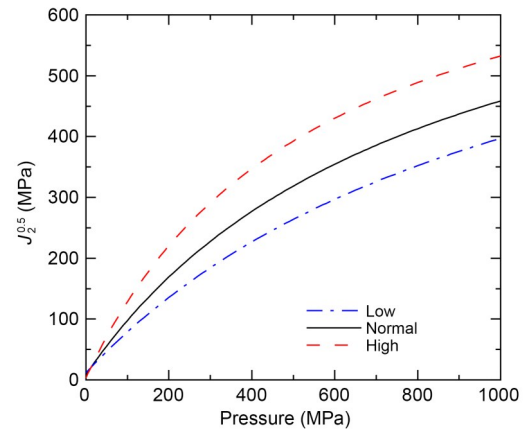


Fig. 15 Influence of a_1 on the shear strength of concrete under high confining pressure

Table 6 Five different shear parameter schemes to investigate the influence of concrete shear behavior on its failure modes and penetration resistance against impacts

Scheme	a_1	a_2	ζ_1	ζ_2
Low	0.8000	$0.025f_c$	0.02	1.5
Med low	0.7000	$0.025f_c$	0.02	1.5
Normal	0.5876	$0.025f_c$	0.02	1.5
Med high	0.5500	$0.025f_c$	0.02	1.5
High	0.5000	$0.025f_c$	0.02	1.5

and empirical formulae where the relation between shear strength and pressure is properly considered in predicting the target resistance and penetration depth (Durban and Masri, 2004; Masri and Durban, 2005; Kong et al., 2017a, 2017b).

As for the failure modes, likewise, the cratering sizes and the scabbing sizes associated with the five different shear parameter schemes (Table 7) are almost the same, which suggests that the shear behavior has very limited influence on the failure modes of the target.

Table 7 Influence of concrete shear behavior on its impact resistance and failure modes

Scheme	300 mm thin concrete targets perforated by 333 m/s projectile			800 mm thick concrete targets penetrated by 347 m/s projectile	
	Residual velocity (m/s)	Cratering size (mm)	Scabbing size (mm)	Penetration depth (mm)	Cratering size (mm)
Low	160.9 (+81.4%)	373.3 (-0.4%)	401.2 (-0.6%)	0.3253 (+20.5%)	416.7 (+4.1%)
Med low	134.3 (+51.4%)	391.4 (+4.4%)	416.5(+3.2%)	0.3033 (+12.4%)	391.4 (-2.2%)
Normal (baseline)	88.7	374.8	403.6	0.2699	400.3
Med high	81.1 (-8.6%)	404.2 (+7.8%)	371.2 (-8.0%)	0.2600 (-3.7%)	403.1 (+0.7%)
High	42.2 (-52.4%)	414.2 (+10.5%)	421.1 (+4.3%)	0.2584 (-4.3%)	406.7 (+1.6%)

Values given in brackets refer to the differences relative to the 'Normal' scheme

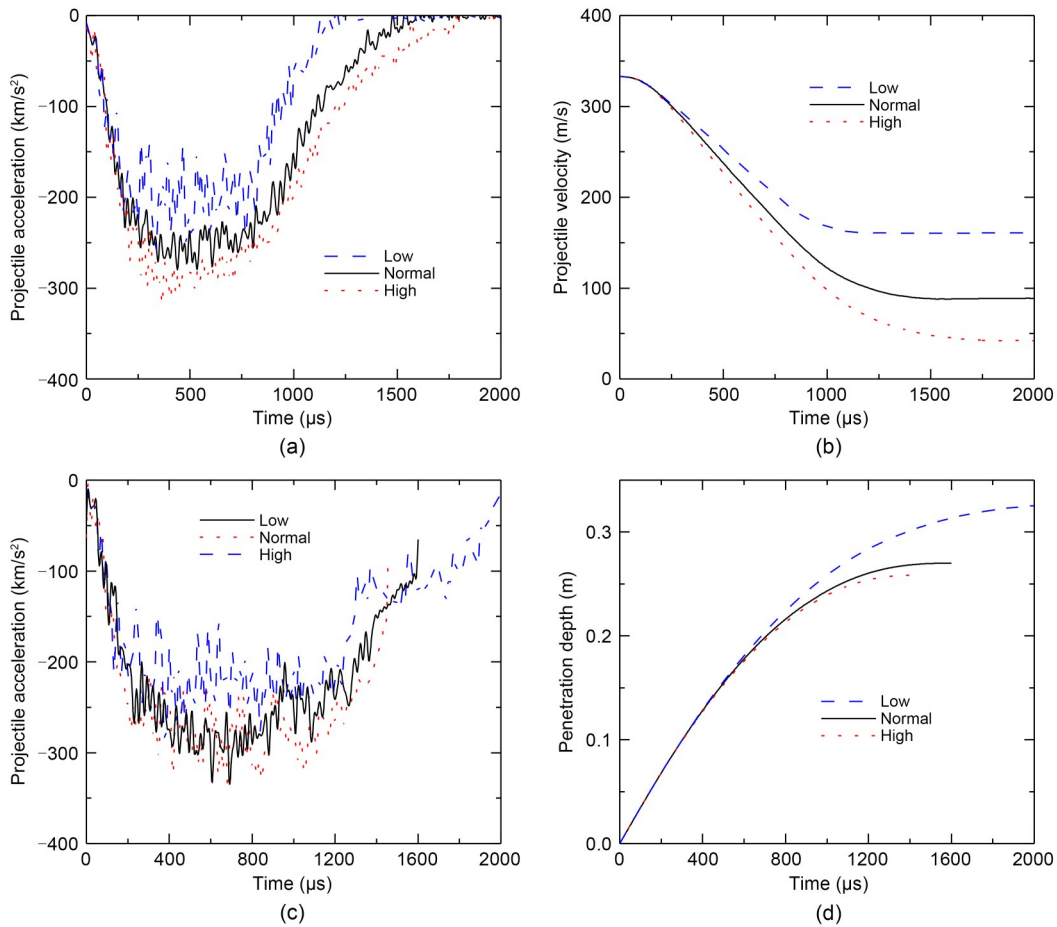


Fig. 16 Influence of concrete shear behavior on the projectile data: projectile acceleration–time histories (a) and projectile velocity–time histories (b) for the perforation case; projectile acceleration–time histories (c) and penetration depth–time histories (d) for the penetration case

5 Discussion and conclusions

By arranging a series of numerical simulations, the individual influence of tensile, volumetric, and shear behaviors of the concrete target on its ballistic performances has been studied. This can be achieved thanks to the well-developed Huang et al. (2021)'s concrete model, where three damage mechanisms have been considered. The two major points, especially the detailed four aspects discussed in Section 1 should be reconsidered based on the numerical results.

The first aspect relates to the damage mechanisms that control the failure modes of the target. Our findings show that the formation of the cratering on the front face and the scabbing on the rear face are mainly dominated by the tensile behavior, and the shear behavior and the volumetric behavior are relatively

unimportant. However, the second tunneling stage in the center of the target is primarily governed by the shear behavior and the volumetric behavior. These findings are consistent with some of the existing research (Hanchak et al., 1992; Huang et al., 2005; Leppänen, 2006; Forquin et al., 2015; Kong et al., 2016).

The second aspect also relates to the damage mechanisms and is focused on the damage due to pore collapse under high pressure. On the one hand, our results and some previous research (Yankelevsky, 1997; Forquin et al., 2008, 2015) revealed the high pressure during the second tunneling stage. On the other hand, a great loss of material properties due to pore collapse under high pressure has been reported by experiments (Cui et al., 2017). Despite this, few numerical studies have considered this damage mechanism. In this study, Huang et al. (2021)'s concrete

model is adopted and the hydrostatic damage is proposed to account for this damage mechanism. Our results clearly capture the hydrostatic damage due to pore collapse under high pressure which is totally distributed in the tunnel.

The third aspect relates to the target resistance and is focused on whether the unconfined compressive strength is sufficient to be the major factor considered in many analytical models and empirical formulae or whether the complex shear and volumetric behaviors considered in the analytical models are necessary. It should be pointed out that abundant numerical simulations were performed in this study with concrete targets of different volumetric behaviors and shear behaviors, as shown in Sections 4.2 and 4.3, respectively. While the unconfined compressive strengths of the targets in different simulations are identical, our findings show that both the residual velocities and penetration depths in different simulations exhibit great discrepancies, with the residual velocities for the perforation case varying from 25.0 to 160.9 m/s, and the penetration depths for the penetration case ranging between 0.2384 and 0.3253 m. These findings suggest that the unconfined compressive strength should not be thought of as the major factor in the target resistance. More complex shear behaviors under triaxial compression stress states as well as volumetric behaviors under hydrostatic loading states should be considered. These conclusions are consistent with some of the existing research (Hanchak et al., 1992; Forquin et al., 2008, 2015; Yankelevsky, 2017).

The fourth aspect also relates to the target resistance and is focused on the influence of the tensile behavior. The opinion that the tensile behavior is not important for the target resistance (Leppänen 2006; Kong et al., 2016) is questioned by the findings obtained in this study. The results in Section 4.1 clearly show that the tensile behavior plays a key role in affecting the target resistance—mainly during the third scabbing stage for a perforation case. The residual velocity of the projectile may vary from 42.5 to 131.3 m/s for different tensile behaviors. For the penetration case where the third scabbing stage is absent, the influence of the tensile behavior on the target resistance can be ignored.

It must be pointed out that the failure mechanisms behind the failure modes of the concrete target

should be different for low-velocity impacts and high-velocity impacts. This study focuses only on low-velocity impacts and so high-velocity or ultrahigh-velocity impacts should be considered in the future. Besides, for high-velocity impacts, there is another factor involved in the target resistance: the velocity inertia. Whether the velocity inertia is necessary when formulating the target resistance is still an open subject. Besides, the conclusions reached are only appropriate for conventional concrete, and future efforts are still need for fiber-reinforced concrete and ultrahigh-performance concrete.

Some other conclusions of this study are presented as follows. Huang et al. (2021)'s concrete model has been demonstrated and can be used in ballistic simulations. The major target resistance comes from the second tunneling stage, where the projectile acceleration is almost constant for low-velocity impacts.

Acknowledgments

This work is supported by the Basic Science Center Program for Multiphase Evolution in Hypergravity of the National Natural Science Foundation of China (No. 51988101) and the Postdoctoral Fellowship Program of China Postdoctoral Science Foundation (No. GZC20232338).

Author contributions

Xieping HUANG designed the research. Shen LIU and Xieping HUANG processed the corresponding data. Shen LIU wrote the first draft of the manuscript. Xieping HUANG revised and edited the final version. Xiangzhen KONG and Qin FANG proofread and validated the manuscript.

Conflict of interest

Shen LIU, Xieping HUANG, Xiangzhen KONG, and Qin FANG declare that they have no conflict of interest.

References

- Batzle ML, Simmons G, Siegfried RW, 1980. Microcrack closure in rocks under stress: direct observation. *Journal of Geophysical Research: Solid Earth*, 85(B12):7072-7090. <https://doi.org/10.1029/JB085iB12p07072>
- Beppu M, Miwa K, Itoh M, et al., 2008. Damage evaluation of concrete plates by high-velocity impact. *International Journal of Impact Engineering*, 35(12):1419-1426. <https://doi.org/10.1016/j.ijimpeng.2008.07.021>
- Chen XW, Li XL, Huang FL, et al., 2008. Normal perforation of reinforced concrete target by rigid projectile. *International Journal of Impact Engineering*, 35(10):1119-1129. <https://doi.org/10.1016/j.ijimpeng.2008.01.002>
- Cui J, Hao H, Shi YC, et al., 2017. Experimental study of

- concrete damage under high hydrostatic pressure. *Cement and Concrete Research*, 100:140-152.
<https://doi.org/10.1016/j.cemconres.2017.06.005>
- de Maio U, Greco F, Leonetti L, et al., 2022. A cohesive fracture model for predicting crack spacing and crack width in reinforced concrete structures. *Engineering Failure Analysis*, 139:106452.
<https://doi.org/10.1016/j.engfailanal.2022.106452>
- Durban D, Masri R, 2004. Dynamic spherical cavity expansion in a pressure sensitive elastoplastic medium. *International Journal of Solids and Structures*, 41(20):5697-5716.
<https://doi.org/10.1016/j.ijsolstr.2004.03.009>
- Feng J, Song ML, Sun WW, et al., 2018. Thick plain concrete targets subjected to high speed penetration of 30CrMnSiNi2A steel projectiles: tests and analyses. *International Journal of Impact Engineering*, 122:305-317.
<https://doi.org/10.1016/j.ijimpeng.2018.09.005>
- Forquin P, Arias A, Zaera R, 2008. Role of porosity in controlling the mechanical and impact behaviours of cement-based materials. *International Journal of Impact Engineering*, 35(3):133-146.
<https://doi.org/10.1016/j.ijimpeng.2007.01.002>
- Forquin P, Sallier L, Pontiroli C, 2015. A numerical study on the influence of free water content on the ballistic performances of plain concrete targets. *Mechanics of Materials*, 89:176-189.
<https://doi.org/10.1016/j.mechmat.2015.02.016>
- Forrestal MJ, Altman BS, Cargile JD, et al., 1994. An empirical equation for penetration depth of ogive-nose projectiles into concrete targets. *International Journal of Impact Engineering*, 15(4):395-405.
[https://doi.org/10.1016/0734-743X\(94\)80024-4](https://doi.org/10.1016/0734-743X(94)80024-4)
- Forrestal MJ, Frew DJ, Hanchak SJ, et al., 1996. Penetration of grout and concrete targets with ogive-nose steel projectiles. *International Journal of Impact Engineering*, 18(5):465-476.
[https://doi.org/10.1016/0734-743X\(95\)00048-F](https://doi.org/10.1016/0734-743X(95)00048-F)
- Goswami A, Adhikary SD, Li B, 2019. Predicting the punching shear failure of concrete slabs under low velocity impact loading. *Engineering Structures*, 184:37-51.
<https://doi.org/10.1016/j.engstruct.2019.01.081>
- Hanchak SJ, Forrestal MJ, Young ER, et al., 1992. Perforation of concrete slabs with 48 MPa (7 ksi) and 140 MPa (20 ksi) unconfined compressive strengths. *International Journal of Impact Engineering*, 12(1):1-7.
[https://doi.org/10.1016/0734-743X\(92\)90282-X](https://doi.org/10.1016/0734-743X(92)90282-X)
- Holmquist TJ, Johnson GR, Cook WH, 1993. A computational constitutive model for concrete subjected to large strains, high strain rates, and high pressures. Proceedings of the 14th International Symposium on Ballistics, p.591-600.
- Hou ZG, 2006. Research on Concrete Strength Under Triaxial Stresses. MS Thesis, Hebei University of Technology, Tianjin, China (in Chinese).
- Huang FL, Wu HJ, Jin QK, et al., 2005. A numerical simulation on the perforation of reinforced concrete targets. *International Journal of Impact Engineering*, 32(1-4):173-187.
<https://doi.org/10.1016/j.ijimpeng.2005.05.009>
- Huang XP, Kong XZ, Chen ZY, et al., 2020. A computational constitutive model for rock in hydrocode. *International Journal of Impact Engineering*, 145:103687.
<https://doi.org/10.1016/j.ijimpeng.2020.103687>
- Huang XP, Kong XZ, Chen ZY, et al., 2021. A plastic-damage model for rock-like materials focused on damage mechanisms under high pressure. *Computers and Geotechnics*, 137:104263.
<https://doi.org/10.1016/j.compgeo.2021.104263>
- Kong XZ, Fang Q, Wu H, et al., 2016. Numerical predictions of cratering and scabbing in concrete slabs subjected to projectile impact using a modified version of HJC material model. *International Journal of Impact Engineering*, 95:61-71.
<https://doi.org/10.1016/j.ijimpeng.2016.04.014>
- Kong XZ, Wu H, Fang Q, et al., 2017a. Rigid and eroding projectile penetration into concrete targets based on an extended dynamic cavity expansion model. *International Journal of Impact Engineering*, 100:13-22.
<https://doi.org/10.1016/j.ijimpeng.2016.10.005>
- Kong XZ, Wu H, Fang Q, et al., 2017b. Projectile penetration into mortar targets with a broad range of striking velocities: test and analyses. *International Journal of Impact Engineering*, 106:18-29.
<https://doi.org/10.1016/j.ijimpeng.2017.02.022>
- Kong XZ, Fang Q, Chen L, et al., 2018. A new material model for concrete subjected to intense dynamic loadings. *International Journal of Impact Engineering*, 120:60-78.
<https://doi.org/10.1016/j.ijimpeng.2018.05.006>
- Leppänen J, 2006. Concrete subjected to projectile and fragment impacts: modelling of crack softening and strain rate dependency in tension. *International Journal of Impact Engineering*, 32(11):1828-1841.
<https://doi.org/10.1016/j.ijimpeng.2005.06.005>
- Li JZ, Lv ZJ, Zhang HS, et al., 2013. Perforation experiments of concrete targets with residual velocity measurements. *International Journal of Impact Engineering*, 57:1-6.
<https://doi.org/10.1016/j.ijimpeng.2013.01.007>
- Li QM, Reid SR, Wen HM, et al., 2005. Local impact effects of hard missiles on concrete targets. *International Journal of Impact Engineering*, 32(1-4):224-284.
<https://doi.org/10.1016/j.ijimpeng.2005.04.005>
- Liu J, Wu CQ, Li J, et al., 2021. Projectile impact resistance of fibre-reinforced geopolymer-based ultra-high performance concrete (G-UHPC). *Construction and Building Materials*, 290:123189.
<https://doi.org/10.1016/j.conbuildmat.2021.123189>
- Masri R, Durban D, 2005. Dynamic spherical cavity expansion in an elastoplastic compressible Mises solid. *Journal of Applied Mechanics*, 72(6):887-898.
<https://doi.org/10.1115/1.1985428>
- Nguyen KD, Thanh CL, Vogel F, et al., 2022. Crack propagation in quasi-brittle materials by fourth-order phase-field cohesive zone model. *Theoretical and Applied Fracture Mechanics*, 118:103236.
<https://doi.org/10.1016/j.tafmec.2021.103236>
- Rajput A, Iqbal MA, Gupta NK, 2018. Ballistic performances

- of concrete targets subjected to long projectile impact. *Thin-Walled Structures*, 126:171-181.
<https://doi.org/10.1016/j.tws.2017.01.021>
- Rosenberg Z, Dekel E, 2010. The deep penetration of concrete targets by rigid rods-revisited. *International Journal of Protective Structures*, 1(1):125-144.
<https://doi.org/10.1260/2041-4196.1.1.125>
- Rosenberg Z, Kositski R, 2016. Modeling the penetration and perforation of concrete targets by rigid projectiles. *International Journal of Protective Structures*, 7(2):157-178.
<https://doi.org/10.1177/2041419616632422>
- Rossi P, 1991. A physical phenomenon which can explain the mechanical behaviour of concrete under high strain rates. *Materials and Structures*, 24(6):422-424.
<https://doi.org/10.1007/BF02472015>
- Taylor LM, Chen EP, Kuszmaul JS, 1986. Microcrack-induced damage accumulation in brittle rock under dynamic loading. *Computer Methods in Applied Mechanics and Engineering*, 55(3):301-320.
[https://doi.org/10.1016/0045-7825\(86\)90057-5](https://doi.org/10.1016/0045-7825(86)90057-5)
- Wang ZL, Li YC, Shen RF, et al., 2007. Numerical study on craters and penetration of concrete slab by ogive-nose steel projectile. *Computers and Geotechnics*, 34(1):1-9.
<https://doi.org/10.1016/j.compgeo.2006.09.001>
- Xie HP, Dong YL, Li SP, 1996. Study of a constitutive model of elasto plastic damage of concrete in axial compression test under different pressures. *Journal of China Coal Society*, 21(3):265-270 (in Chinese).
- Xing HZ, Zhao J, Wu G, et al., 2020. Perforation model of thin rock slab subjected to rigid projectile impact at an intermediate velocity. *International Journal of Impact Engineering*, 139:103536.
<https://doi.org/10.1016/j.ijimpeng.2020.103536>
- Xiong YB, 2009. Research on Constitutive Parameters of Concrete Based on the Johnson-Holmquist Concrete Model. MS Thesis, Northwest Institute of Nuclear Technology, Xi'an, China (in Chinese).
- Xu LZ, Ren WK, Wang XD, et al., 2021. Analytical investigation on deformation of PELE projectile and opening damage to concrete target. *Thin-Walled Structures*, 161:107408.
<https://doi.org/10.1016/j.tws.2020.107408>
- Yankelevsky DZ, 1997. Local response of concrete slabs to low velocity missile impact. *International Journal of Impact Engineering*, 19(4):331-343.
[https://doi.org/10.1016/S0734-743X\(96\)00041-3](https://doi.org/10.1016/S0734-743X(96)00041-3)
- Yankelevsky DZ, 2017. Resistance of a concrete target to penetration of a rigid projectile-revisited. *International Journal of Impact Engineering*, 106:30-43.
<https://doi.org/10.1016/j.ijimpeng.2017.02.021>
- Zhao FQ, Wen HM, 2018. Effect of free water content on the penetration of concrete. *International Journal of Impact Engineering*, 121:180-190.
<https://doi.org/10.1016/j.ijimpeng.2018.06.007>
- Zhu C, Arson C, 2014. A thermo-mechanical damage model for rock stiffness during anisotropic crack opening and closure. *Acta Geotechnica*, 9(5):847-867.